Optimising Multi-frame ADF-STEM for High-precision Atomic-resolution Strain Mapping

Lewys Jones[1*], Sigurd Wenner[2], Magnus Nord[2], Per Harald Ninive[3], Ole Martin Løvvik[4], Randi Holmestad[2] and Peter D. Nellist[1]

[1] *Department of Materials, University of Oxford, Oxford, UK, OX13PH*

[2] *Department of Physics, NTNU- Norwegian University of Science and Technology, Trondheim, Norway, NO-7491*

[3] *NTNU- Norwegian University of Science and Technology, Gjøvik, Norway, NO-2815*

[4] *SINTEF Materials and Chemistry, Oslo, Norway, NO-0314*

* e-mail address: lewys.jones@materials.ox.ac.uk

Annular dark-field scanning transmission electron microscopy is a powerful tool to study crystal defects at the atomic scale but historically single slow-scanned frames have been plagued by low-frequency scanning-distortions prohibiting accurate strain mapping at atomic resolution. Recently, multi-frame acquisition approaches combined with post-processing have demonstrated significant improvements in strain precision, but the optimum number of frames to record has not been explored. Here we use a non-rigid image registration procedure before applying established strain mapping methods. We determine how, for a fixed total electron-budget, the available dose should be fractionated for maximum strain mapping precision. We find that reductions in scanning-artefacts of more than 70% are achievable with image series of 20-30 frames in length. For our setup, series longer than 30 frames showed little further improvement. As an application, the strain field around an aluminium alloy precipitate was studied, from which our optimised approach yields data whos strain accuracy is verified using density functional theory.

Keywords: ADF-STEM, experiment design, strain in crystals/solids, aluminium alloys, density functional calculations.

Introduction

The measurement of lattice distortion and strain in materials at the nanoscale presents an important characterisation challenge. Strain is crucial in controlling the functional, electrical and mechanical properties of materials, and strain field design can unlock the engineering of new material properties, including in quantum-dots [1], semiconductor transistors [2], ferroelectrics [3], flexoelectrics [4], high-temperature superconductors [5] and alloy development [6]. High-resolution electron microscopy techniques can map strain information; however, the finite resolution and signal-to-noise ratio (SNR) of experimental images makes a quantitative measurement of these subtle displacements very challenging. Current experimental approaches include; conventional transmission electron microscopy (CTEM) [7–9], convergent-beam [10], nano-beam [11] or nano-precession [12] electron diffraction (CBED, NBED, NPED), dark-field electron holography [13] (DFEH), and annular dark-field scanning transmission electron microscopy (ADF-STEM) [14–16]. Concise reviews of these methods can be found elsewhere [17,18]; but notably, each of these methods come with their own unique complications. With CTEM, careful choice of imaging parameters must be used to avoid image artefacts or contrast inversions from (for example) sample-tilt, sample-thickness, defocus or aberration changes. CBED strain measurements can require significant sample tilt to achieve high-precision and can be vulnerable to crystal plane bending, while DFEH, NBED and NPED techniques each require additional hardware (a bi-prism, an additional condenser lens, and precession coils respectively) and more involved off-line data processing. Lastly, in STEM the serial nature of the image raster means that environmental effects can distort the image fidelity [19–21] and the necessary atomic resolution generally requires aberration correction.

Of the methods above, there has been increased interest recently in measuring strain from ADF-STEM images to make use of their Z-contrast and incoherent nature. The development of high-brightness electron sources and aberration correctors has improved image-resolution, while improvements in power-supply stability and acoustic isolation [19] have reduced problems from 50(60)Hz electrical, and few-kHz acoustic, *scan-noise* artefacts respectively [20,22]. As a result, and taking the nomenclature from [21], our attention now turns to the far harder to isolate low-frequency (few Hz) *scan-distortion* and unavoidable Poisson counting-noise. Strain mapping using ADF-STEM will only reach its full potential if the deleterious effects of low-frequency scanning-distortion can be minimised.

Previous scan-distortion correction efforts can be grouped into those using reference data or those using frame-averaging. Reference approaches have required instrument mode changes [23], or assumptions to be made that distortions remain constant between line-synced images recorded at different times [24,25], or within whole scan-lines of an image [16]. However, as practical environmental distortions cannot be assumed to be reproducible, such methods often retain scan-distortion artefacts even in their corrected data [16,24]. Alternative approaches using averaged multi-frame data may perform

better and show increased signal-noise ratio but can have different limitations. Moire based methods surveying larger fields of view cannot visualise strain around localised defects [2,26], while simple rigid-alignment [15] or the more advanced rigid-plus-affine approaches[27], do not incorporate localised non-linear scanning-distortions [21,28]. These distortions, if not countered, then lead to a worsening of image resolution during averaging [29]. Lastly, unconstrained non-rigid registration [30] can lead to artefacts at sample edges [21] and appears to converge more slowly (Figure 1).

In this work we do not introduce a new method of strain measurement, but rather we evaluate how to best utilise a fixed electron-dose-budget in the context of multi-frame acquisitions. We use existing methods of strain mapping from the literature to evaluate image precision, such as Fourier-space geometric phase analysis (GPA), which is fast to compute, but fundamentally not atomic-resolution [8], or real-space peak finding (atomic-resolution but more computationally intensive to extract) [14];. Non-rigid registration of multi-frame ADF data is performed using the Smart Align algorithm [21]; this approach does not make assumptions about crystal-periodicity or crystal-orientation, does not require that scanning-distortions remain constant across whole scan-frames or scan-lines, is able to incorporate non-linear distortion correction, and is robust to sample edges and local defects.

The dose-fractionation optimisation is evaluated using a model $SrTiO_3$ image series before it is deployed to obtain high-quality ADF images of an AlMgSi precipitate. These are then used to demonstrate the ability to extract strain data that is directly comparable with density functional theory (DFT) calculations. The experiment-design method presented here for spatial-precision optimisation is general across various STEM detector geometries; including, medium-angle dark-field (MAADF) [31], annular bright-field (ABF) [32], or even spectrum-imaging time-series [33].

Optimising Dose Fractionation

A collection of ADF-STEM image series were recorded from a [110] oriented crystal of $SrTiO_3$ (STO) with a total fixed dose, but differently fractionated across increasing numbers of frames. Imaging was performed using a double aberration-corrected JEOL ARM-200CF; for the STO sample the acceleration was set to 200 kV to obtain a high spatial resolution. Total electron-dose was maintained by varying the pixel dwell-time. The series recorded were for example, 1x 40μs, 4x10μs, etc. through to 40x1μs. Other variables such as fly-back settling time or field of view [17] may affect the apparent strain, but these were all kept constant throughout this investigation. The data were realigned and non-rigid registered using the STEM robust mode of the Smart Align method [21] and then GPA was used to measure the apparent strain. Example ADF data recorded with differing dwell-times are shown in Figure 1 (top row).
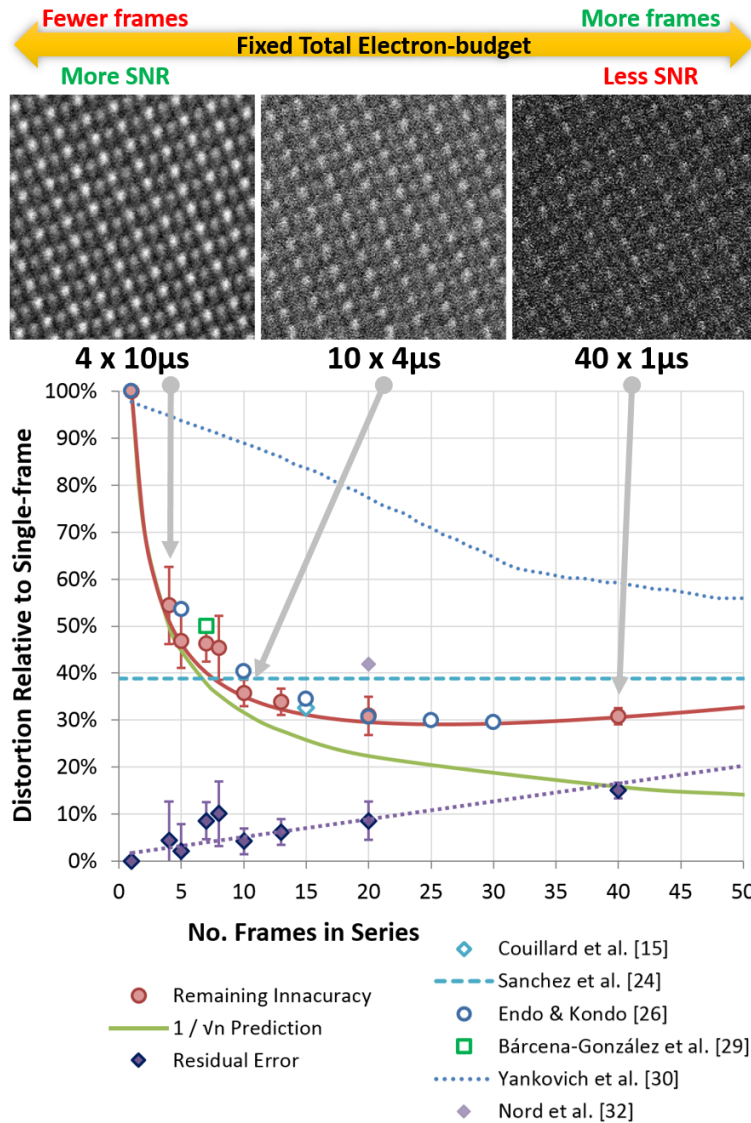
Figure 1. Illustration of the experimental optimisation for a fixed total electron-dose; top row shows 200x200px (1.84nm^2) crops from example frames from ADF-series of [110] STO with dwell times of 10µs, 4µs, and 1µs. Bottom, the distortion magnitude relative to a single 40µs dwell-time slow-scanned frame. Filled circles show the reduction in relative scan-distortion with increasing number of STEM frames (fixed total dose). Five additional reference data are also shown normalised from references [15,24,26,29,30,32].

For a fixed total electron-dose budget we are able to record more frames when the pixel dwell-time is reduced, though the SNR of each of these individual frames is necessarily reduced. After each ADF-series has been non-rigidly aligned and averaged, ε_{yy} plots were calculated using GPA. Because of the inherent Fourier-filtering of GPA, GPA is highly robust to Poissonian noise, and is hence a robust and useful tool here for analysing the distortions across the varying dose-series. Figure 2a) shows an example of such a plot for a conventional single scan with a 40µs dwell-time. The strain in this large defect-free single crystal should necessarily be zero, as a result the ε_{yy} plot (which scrutinises the slow-scan direction) acts as

a very sensitive metric of any imaging distortions present. As this ε_{yy} plot is purely a measure of scanning distortion, it does not depend on crystal orientation.
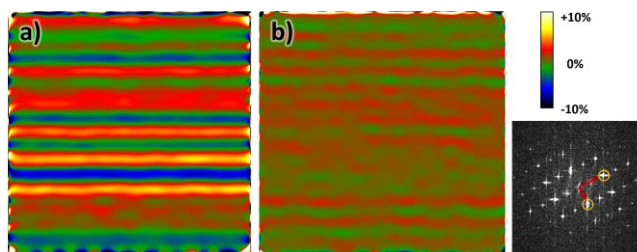

Figure 2. Erroneous ε_{yy} strain plots caused by scan-distortion from, a) the single 40µs scan and b) the non-rigid realigned restoration of 20x2µs scans (same total dose). After processing, the dose sharing multi-frame approach shows significant improvement in accuracy. FFT shows the spots selected for GPA.

For each frame of the individual ADF scans in each series, the average standard deviation of ε_{yy} was measured to be 2.11% with no trend observed with respect to scan-speed (see supplemental information at [**URL**]). This is effectively the baseline measure of the combined stability of the microscope, sample, and EM-suite. The average ε_{yy} standard deviation of 2.11% reflects the environmental conditions present of the day of the experiments; from this we would expect genuine strains of less than 2% to be difficult to observe over these artefacts.

Next, each of the image series were non-rigid registered using the Smart Align algorithm [21], averaged, and analysed in the same way. Figure 2 b) shows an example ε_{yy} plot after scan correction and averaging. To evaluate the improvement in strain-mapping precision, the 'distortion relative to a single-frame' is plotted in Figure 1. This is defined as the standard deviation in ε_{yy} of the corrected data, divided by the standard deviation of ε_{yy} from the single-frame. We find that, when moving to a dose-fractionated multi-frame regime, the scan-correction and averaging approach reduced the ε_{yy} standard deviation for all dose fractionation cases investigated here, Figure 1 (filled circles).

We can also consider what we expect to be the ultimate performance limit for this approach; if strain mapping in ADF is predominantly concerned with the reliable observation of Gaussian-like atomic columns, the precision of their position estimation is then the fundamental limit. For multi-frame data, the precision in the position-estimation of the sum of Guassians shifted randomly about some true centre, would be expected to improve inversely with the square root of the number of observations, that is a classic $1/\sqrt{n}$ behaviour, where n is the number of frames in the average. This $1/\sqrt{n}$ prediction is indicated in Figure 1 (solid green line). The difference between the obtained improvement and the $1/\sqrt{n}$ limit scales approximately linearly with the number of frames (increasing dose fractionation) and adding together the $1/\sqrt{n}$ and linear terms, we find a model which describes our experimental data well. One explanation for this extra linear term, may be that our data with the very lowest electron dose per frame perhaps cannot be completely re-registered, or that at such low dose

some other source of read-out noise (perhaps from the amplification system) begins to limit the data quality. Previous studies have found that dwell-times faster than 2µs begin to show noticeable fast-scan streaking, while below 0.5µs these images become largely unusable [34]. More recently this has been explained in terms of the scintillator afterglow time constant [35,36]. This is consistent with the lack of improvement seen here between 20 and 40 times fractionation of our constant total dose. For this reason the authors here recommend that, using the current generation of detectors/photomultipliers, 1.5µs should be considered as a minimum dwell-time for ADF imaging.

Using the metric of 'distortion relative to a single frame', also allows us to compare our new results with previous distortion-correction approaches from the literature; the normalisation of each literature data is described in the supplementary information. The reduction in image distortion achieved here is consistent with simple averaging and Moire approaches [15,26,29], but with the advantage that it can be used for aperiodic features (defects) and does not lose spatial resolution on averaging as is the case if non-linear distortions go uncorrected. Compared with approaches using line-synced reference images [24,25], the approach followed here delivered a better performance when eight or more images are used for the distortion correction. Furthermore, the conditions are more flexible here as there is no need for the data to be line-synced and no second sample is needed for the reference. Lastly, compared with isotropic non-rigid registration methods [30], our STEM-bespoke scan-constrained method requires significantly fewer frames to yield a similar relative improvement (e.g. ~4 frames versus ~100 frames for a 50% improvement). As correction of scan-noise (artefacts within scan-lines) does not improve strain mapping precision (dependant on artefacts across scan-lines), these methods do not appear on Figure 1 [20,22].

Our optimisation approach then suggests that, for the conditions used here, the total electron-dose should be shared across 20-30 frames yielding a distortion reduction to below 30% of the original. With the environmental distortions present on the day of the experiment, this is equivalent to an ε_{yy} precision improvement from ±2.11% to ±0.6%. For dose-fractionations across more than 30 frames, no significant further improvement was observed. Users may need to determine the optimum dose-fractionation for their own samples, instrument, or chosen total dose, but the approach followed here is general. This approach then yielded the optimised acquisition conditions for the next phase of experiments.

Application to Alloy Precipitate Strain Measurement

Once acquisition parameters were optimised, ADF imaging was repeated on a [100] oriented aluminium crystal containing needle-shaped β'' type AlMgSi precipitates imaged along their long axis [6,37]. Samples were prepared by electro-polishing following the method in [38] from a material annealed at 195°C for 4 hours after homogenisation. EELS t/λ measurements allow for the thickness to be evaluated, and the highest-quality images were obtained from the thinnest regions of the foil

where specimen thickness was approximately 20-40nm. For the Al-alloy imaging the accelerating voltage was set to 80 kV to avoid knock-on damage to the precipitates. For more details on microscope parameters, see the supplementary material. A precipitate running through the whole thickness of the foil was selected that was far from any others and can be treated as being alone in the Al matrix. Owing to the very high in-plane strain there may be some corresponding relaxation in the surface normal direction. Specimen relaxation could therefore give a small underestimate of the in-plane strain in the experimental observations. Further details may be found in previous publications [39,40]. 38 frames (2048x2048 pix) with 1.6μs dwell time were recorded before alignment using the Smart Align algorithm [21]. Figure 3 a) shows the central region from an average ADF-STEM frame (wider view in supplemental information).
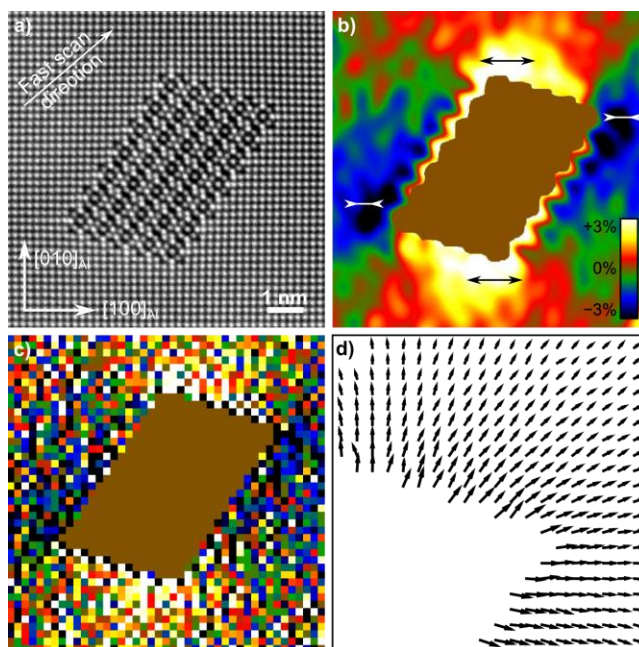

Figure 3. a) Average ADF image restored by the Smart Align algorithm. The field of view is about 1/8 of the scan area (the whole field is shown in the supplement). b) εxx plot measured using GPA with a 0.6 nm mask, and c) by real-space peak position measurement (same colour scale as b)). d) Atomic displacements (relative to a perfect lattice) from the upper right part of the image. The arrows show the direction of the displacement, and are scaled larger by 3.1x with respect to magnitude which varies in the range 0–0.08 nm.

The ADF image in Figure 3a) yields easily interpretable contrast, with both the structural unit and the edge of the precipitate readily identified; this is in contrast with HRTEM (see supplementary information) where image contrast can be difficult to interpret. Moreover, while not performed here, STEM also allows for simultaneous chemical analysis at atomic resolution [33].

Precipitate strain fields were analysed by GPA and real-space peak-position approaches (Figure 3) and compared with predictions from DFT, Figure 4. For the real-space analysis these strains are the differential displacements divided by the inter-column spacing. As DFT computation scales with model size cubed, a 12×12×1 unit supercell (576 atoms) was used.

Four β'' formula units were introduced by substituting Al according to established composition and orientation relationships [41,42]. The precipitates were thus finite (but periodic) in the cross-sectional plane and infinite along the needle direction ([001]$_{Al}$), Figure 4.
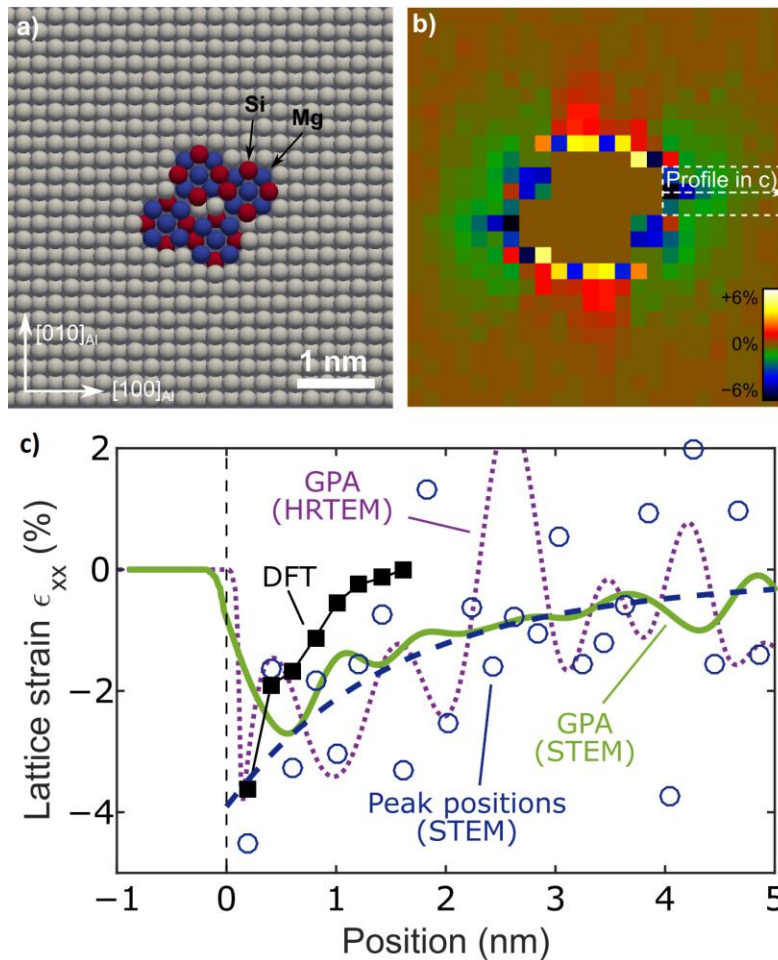

Figure 4. a) Schematic of the model used for the DFT relaxation, b) the resulting ε$_{xx}$ plot, and c) comparison of strain profiles outside a precipitate corner from STEM-GPA (solid line), STEM peak-positions (open circles), DFT (solid squares), and HRTEM GPA (dashed line).

The strain analyses show that the aluminium columns are displaced away from the precipitate by up to 0.08nm in a radial fashion, which is appropriate for such a needle-shaped precipitate with a positive misfit with the lattice [43]. These plots highlight however some differences between real- and reciprocal-space approaches; for GPA, the intrinsic limits of the mask used yield some periodic artefacts along the precipitate edge, while the real-space analysis, though at a better spatial resolution, exhibits more noise. Because of this noise a least-squares fit to the strain field around an cylindrical Eshelby inclusion is shown, yielding a scaling factor k = 0.864 nm^3 [43]. This real-space trend-line very closely reproduces the DFT predicted misfit at the first Al-matrix atomic-column (DFT = -3.633%, fit = -3.467%); this difference of 0.166% corresponds to a discrepancy of 0.34pm. After this first aluminium lattice position, the observed strain decays faster for the smaller DFT

simulation, reaching zero after approximately 1.5nm, versus ~6nm for the experiment (see supplement). This is because of the finite supercell size of the atomistic model – the superposition of periodic images of the precipitate more or less cancels out at the supercell boundaries. Owing the computational limitations of DFT it was not possible to increase the size of the supercell beyond 576 atoms at this time without compromising accuracy, but in the future it may be possible to simulate larger cells. While it is not the focus of this work to compare strain measurement techniques, Figure 4 also shows the overall reasonable agreement between GPA and real-space analyses of the same image. However it should be noted that GPA, containing only one Fourier spot within each mask, can never achieve atomic resolution and so appears considerably smoothed relative to the real-space analysis. This effect is especially noticeable at the particle-matrix interface where GPA appreciably underestimates the strain predicted by DFT (GPA gives around 2% compared with around 3.5% for the DFT & real-space analysis).

Lastly, if we take a region in the aluminium matrix from Figure 3b) far from the precipitate and analyse the strain-measurement precision, the standard deviation from non-rigid registered multi-frame ADF images was found to be 0.3%; this is better than the results from the STO owing to the better instrument stability on the day of the experiment. For comparison, an HRTEM image was taken with a pixel-size and field-of-view similar to the ADF data (see supplementary information). The GPA precision from the Al-matrix was found to be 0.9%. This improved to 0.5% for an image recorded with a higher magnification, though this yielded a smaller field of view. In contrast to scanned microscopies, as no scanning-distortions are observed in HRTEM, GPA analysis does not benefit from frame-averaging in the same way. In the literature HRTEM-GPA precisions as good as 0.3% have been reported [9], a precision which we are now able to match with ADF-STEM. This, combined with the ease of interpretation of incoherent (z-contrast) ADF, and the ability to include atomic resolution chemical mapping [44,45], makes multi-frame STEM a key new approach for mapping strain at atomic resolution.

Finally, whilst the multi-frame image alignment and averaging precision improvement is impressive, it should be noted that it is always better to address environmental distortions at source before post-processing.

Conclusions

Recent developments in non-rigid registration have spawned new questions in experiment design. Here fractionation of a fixed total electron-dose was studied with specific attention paid to the accuracy and precision of ADF-STEM strain data. After optimising the experiment design, scanning artefacts were reduced by 70% for series with 20-30 frames.

To test the approach, experimental data were collected from β" precipitates in aluminium. Their experimentally measured strain fields were compared with DFT and found to be in good agreement at the precipitate interface within an accuracy of around 1%. The precision of multi-frame ADF-STEM was found to equal that of HRTEM-GPA for the first time, this

combined with the opportunity for simultaneous atomic-resolution spectroscopy opens exciting avenues in alloy microstructure characterisation by STEM.

Further work in calculating the interaction between dislocations in Al and the strain field originating from precipitates of different sizes and atomic structure is underway [31]. This will help to refine existing models of precipitation strengthening for both fundamental and industrial research.

———

References

[1]   F. Guffarth, R. Heitz, A. Schliwa, O. Stier, N.N. Ledentsov, A.R. Kovsh, et al., Strain engineering of self-organized InAs quantum dots, Phys. Rev. B. 64 (2001) 85305. doi:10.1103/PhysRevB.64.085305.

[2]   S. Kim, Y. Kondo, K. Lee, G. Byun, J. Jung Kim, S. Lee, et al., Quantitative measurement of strain field in strained-channel-transistor arrays by scanning moiré fringe imaging, Appl. Phys. Lett. 103 (2013) 33523. doi:10.1063/1.4816286.

[3]   P. Gao, C.T. Nelson, J.R. Jokisaari, S.-H. Baek, C.W. Bark, Y. Zhang, et al., Revealing the role of defects in ferroelectric switching with atomic resolution, Nat. Commun. 2 (2011) 591. doi:10.1038/ncomms1600.

[4]   G. Catalan, a. Lubk, a. H.G. Vlooswijk, E. Snoeck, C. Magen, a. Janssens, et al., Flexoelectric rotation of polarization in ferroelectric thin films, Nat. Mater. 10 (2011) 963–967. doi:10.1038/nmat3141.

[5]   a. Llordés, A. Palau, J. Gázquez, M. Coll, R. Vlad, A. Pomar, et al., Nanoscale strain-induced pair suppression as a vortex-pinning mechanism in high-temperature superconductors, Nat. Mater. 11 (2012) 329–336. doi:10.1038/nmat3247.

[6]   E.A. Mørtsell, C.D. Marioara, S.J. Andersen, J. Røyset, O. Reiso, R. Holmestad, Effects of Germanium, Copper, and Silver Substitutions on Hardness and Microstructure in Lean Al-Mg-Si Alloys, Metall. Mater. Trans. A. 46 (2015) 4369–4379. doi:10.1007/s11661-015-3039-5.

[7]   H. Seitz, M. Seibt, F.H. Baumann, K. Ahlborn, W. Schröter, Quantitative strain mapping using high-resolution electron microscopy, Phys. Status Solidi. 150 (1995) 625–634. doi:10.1002/pssa.2211500206.

[8]   M.J. Hÿtch, E. Snoeck, R. Kilaas, Quantitative measurement of displacement and strain fields from HREM micrographs, Ultramicroscopy. 74 (1998) 131–146. doi:10.1016/S0304-3991(98)00035-7.

[9]   F. Hüe, M.J. Hÿtch, H. Bender, F. Houdellier, A. Claverie, Direct Mapping of Strain in a Strained Silicon Transistor by High-Resolution Electron Microscopy, Phys. Rev. Lett. 100 (2008) 156602.

doi:10.1103/PhysRevLett.100.156602.

[10]   P. Zhang, A. a. Istratov, E.R. Weber, C. Kisielowski, H. He, C. Nelson, et al., Direct strain measurement in a 65 nm node strained silicon transistor by convergent-beam electron diffraction, Appl. Phys. Lett. 89 (2006) 20–23. doi:10.1063/1.2362978.

[11]   V.B. Ozdol, C. Gammer, X.G. Jin, P. Ercius, C. Ophus, J. Ciston, et al., Strain mapping at nanometer resolution using advanced nano-beam electron diffraction, Appl. Phys. Lett. 106 (2015) 253107. doi:10.1063/1.4922994.

[12]   J.-L.L. Rouviere, A. Béché, Y. Martin, T. Denneulin, D. Cooper, A. Béché, et al., Improved strain precision with high spatial resolution using nanobeam precession electron diffraction, Appl. Phys. Lett. 103 (2013) 241913. doi:10.1063/1.4829154.

[13]   A. Béché, J.L.L. Rouvière, J.P.P. Barnes, D. Cooper, Dark field electron holography for strain measurement, Ultramicroscopy. 111 (2011) 227–238. doi:10.1016/j.ultramic.2010.11.030.

[14]   P.L. Galindo, S. Kret, A.M. Sanchez, J.-Y. Laval, A. Yáñez, J. Pizarro, et al., The Peak Pairs algorithm for strain mapping from HRTEM images., Ultramicroscopy. 107 (2007) 1186–93. doi:10.1016/j.ultramic.2007.01.019.

[15]   M. Couillard, G. Radtke, G.A. Botton, Strain fields around dislocation arrays in a Σ9 silicon bicrystal measured by scanning transmission electron microscopy, Philos. Mag. 93 (2013) 1250–1267. doi:10.1080/14786435.2013.778428.

[16]   J.-M. Zuo, A.B. Shah, H. Kim, Y. Meng, W. Gao, J.-L. Rouviére, Lattice and strain analysis of atomic resolution Z-contrast images based on template matching., Ultramicroscopy. 136 (2014) 50–60. doi:10.1016/j.ultramic.2013.07.018.

[17]   D. Cooper, T. Denneulin, N. Bernier, A. Béché, J.-L. Rouvière, Strain mapping of semiconductor specimens with nm-scale resolution in a transmission electron microscope, Micron. 80 (2016) 145–165. doi:10.1016/j.micron.2015.09.001.

[18]   M.J. Hÿtch, A.M. Minor, Observing and measuring strain in nanostructures and devices with transmission electron microscopy, MRS Bull. 39 (2014) 138–146. doi:10.1557/mrs.2014.4.

[19]   D.A. Muller, E.J. Kirkland, M.G. Thomas, J.L. Grazul, L. Fitting, M. Weyland, Room design for high-performance electron microscopy., Ultramicroscopy. 106 (2006) 1033–40. doi:10.1016/j.ultramic.2006.04.017.

[20]   L. Jones, P.D. Nellist, Identifying and Correcting Scan Noise and Drift in the Scanning Transmission Electron Microscope, Microsc. Microanal. 19 (2013) 1050–1060. doi:10.1017/S1431927613001402.

[21]   L. Jones, H. Yang, T.J. Pennycook, M.S.J. Marshall, S. Van Aert, N.D. Browning, et al., Smart Align—a new tool for robust non-rigid registration of scanning microscope data, Adv. Struct. Chem. Imaging. 1 (2015) 8. doi:10.1186/s40679-015-0008-4.

[22]   N. Braidy, Y. Le Bouar, S. Lazar, C. Ricolleau, Correcting scanning instabilities from images of periodic structures., Ultramicroscopy. 118 (2012) 67–76. http://dx.doi.org/10.1016/j.ultramic.2012.04.001 (accessed August 13, 2012).

[23]   A. Recnik, G. Möbus, S. Sturm, IMAGE-WARP: a real-space restoration method for high-resolution STEM images using quantitative HRTEM analysis., Ultramicroscopy. 103 (2005) 285–301. doi:10.1016/j.ultramic.2005.01.003.

[24]   A.M. Sanchez, P.L. Galindo, S. Kret, M. Falke, R. Beanland, P.J. Goodhew, An approach to the systematic distortion correction in aberration-corrected HAADF images., J. Microsc. 221 (2006) 1–7. doi:10.1111/j.1365-2818.2006.01533.x.

[25]   A.M. Sanchez, P.L. Galindo, S. Kret, M. Falke, R. Beanland, P.J. Goodhew, Quantitative Strain Mapping Applied to Aberration-Corrected HAADF Images, Microsc. Microanal. 12 (2006) 285–94. doi:10.1017/S1431927606060363.

[26]   N. Endo, Y. Kondo, Accuracy of Strain in Strain Maps Improved by Averaging Multiple Maps, Microsc. Microanal. 20 (2014) 1068–1069. doi:10.1017/S1431927614007065.

[27]   X. Sang, J.M. LeBeau, Revolving scanning transmission electron microscopy: Correcting sample drift distortion without prior knowledge., Ultramicroscopy. 138C (2013) 28–35. doi:10.1016/j.ultramic.2013.12.004.

[28]   C. Ophus, J. Ciston, C.T. Nelson, Correcting nonlinear drift distortion of scanning probe and scanning transmission electron microscopies from image pairs with orthogonal scan directions, Ultramicroscopy. 162 (2016) 1–9. doi:10.1016/j.ultramic.2015.12.002.

[29]   G. Bárcena-González, M.P. Guerrero-Lebrero, E. Guerrero, D. Fernández-Reyes, D. González, A. Mayoral, et al., Strain mapping accuracy improvement using super-resolution techniques, J. Microsc. 0 (2015) 1–9. doi:10.1111/jmi.12341.

[30]   A.B. Yankovich, B. Berkels, W. Dahmen, P. Binev, S.I. Sanchez, S.A. Bradley, et al., Picometre-precision analysis of scanning transmission electron microscopy images of platinum nanocatalysts, Nat. Commun. 5 (2014). doi:10.1038/ncomms5155.

[31]   S. Wenner, R. Holmestad, Accurately measured precipitate–matrix misfit in an Al–Mg–Si alloy by electron microscopy, Scr. Mater. 118 (2016) 5–8. doi:10.1016/j.scriptamat.2016.02.031.

[32]   M. Nord, P.E. Vullum, I. MacLaren, T. Tybell, R. Holmestad, Atomap: a new software tool for the automated analysis of atomic resolution images using two-dimensional Gaussian fitting, Adv. Struct. Chem. Imaging. 3 (2017) 9. doi:10.1186/s40679-017-0042-5.

[33]   S. Wenner, L. Jones, C.D. Marioara, R. Holmestad, Atomic-resolution chemical mapping of ordered precipitates in Al alloys using energy-dispersive X-ray spectroscopy, Micron. (2017). doi:10.1016/j.micron.2017.02.007.

[34]   J.P. Buban, Q. Ramasse, B. Gipson, N.D. Browning, H. Stahlberg, High-resolution low-dose scanning transmission

electron microscopy., J. Electron Microsc. (Tokyo). 59 (2010) 103–12. doi:10.1093/jmicro/dfp052.

[35]   F.F. Krause, M. Schowalter, T. Grieb, K. Müller-Caspary, T. Mehrtens, A. Rosenauer, Effects of instrument imperfections on quantitative scanning transmission electron microscopy, Ultramicroscopy. 161 (2016) 146–160. doi:10.1016/j.ultramic.2015.10.026.

[36]   X. Sang, J.M. LeBeau, Characterizing the response of a scintillator-based detector to single electrons, Ultramicroscopy. 161 (2016) 3–9. doi:10.1016/j.ultramic.2015.11.008.

[37]   H.W. Zandbergen, S.J. Andersen, J. Jansen, Structure Determination of Mg5Si6 Particles in Al by Dynamic Electron Diffraction Studies, Science (80-.). 277 (1997) 1221–1225. doi:10.1126/science.277.5330.1221.

[38]   S. Wenner, C.D. Marioara, S.J. Andersen, R. Holmestad, Effect of room temperature storage time on precipitation in Al–Mg–Si(–Cu) alloys with different Mg/Si ratios, Int. J. Mater. Res. 103 (2012) 948–954. doi:10.3139/146.110795.

[39]   P.H. Ninive, O.M. Løvvik, A. Strandlie, Density Functional Study of the β″ Phase in Al-Mg-Si Alloys, Metall. Mater. Trans. A. 45 (2014) 2916–2924. doi:10.1007/s11661-014-2214-4.

[40]   P.H. Ninive, A. Strandlie, S. Gulbrandsen-Dahl, W. Lefebvre, C.D. Marioara, S.J. Andersen, et al., Detailed atomistic insight into the β″ phase in Al-Mg-Si alloys, Acta Mater. 69 (2014) 126–134. doi:10.1016/j.actamat.2014.01.052.

[41]   S.J. Andersen, H.W. Zandbergen, J. Jansen, C. Træholt, U. Tundal, O. Reiso, The crystal structure of the β″ phase in Al–Mg–Si alloys, Acta Mater. 46 (1998) 3283–3298. doi:10.1016/S1359-6454(97)00493-X.

[42]   H.S. Hasting, A.G. Frøseth, S.J. Andersen, R. Vissers, J.C. Walmsley, C.D. Marioara, et al., Composition of β[sup ″] precipitates in Al–Mg–Si alloys by atom probe tomography and first principles calculations, J. Appl. Phys. 106 (2009) 123527. doi:10.1063/1.3269714.

[43]   J. Douin, P. Donnadieu, F. Houdellier, Elastic strain around needle-shaped particles embedded in Al matrix, Acta Mater. 58 (2010) 5782–5788. doi:10.1016/j.actamat.2010.06.053.

[44]   S.J. Kang, Y.-W. Kim, M. Kim, J.-M. Zuo, Determination of interfacial atomic structure, misfits and energetics of Ω phase in Al–Cu–Mg–Ag alloy, Acta Mater. 81 (2014) 501–511. doi:10.1016/j.actamat.2014.07.074.

[45]   S. Wenner, C.D. Marioara, Q.M. Ramasse, D.-M. Kepaptsoglou, F.S. Hage, R. Holmestad, Atomic-resolution electron energy loss studies of precipitates in an Al–Mg–Si–Cu–Ag alloy, Scr. Mater. 74 (2014) 92–95. doi:10.1016/j.scriptamat.2013.11.007.

Acknowledgments

Author Contributions Statement

LJ designed the optimisation methodology and produced figures 1 and 2; SW recorded the experimental data in figure 3 and performed the alloy strain analyses; MN recorded the STO experimental data; PHN and OML configured and executed the DFT calculations; RH and PDN directed the research programme. All authors contributed to writing and proofing the manuscript.